Chance-Constrained Rollover-Free Manipulation Planning with Uncertain Payload Mass

Jiazhi Song[1], *Student Member, IEEE*, Antoine Petraki[1], Brandon J. DeHart[2] and Inna Sharf[3], *Member, IEEE*

***Abstract*—This paper presents a chance-constrained rollover-free manipulation planning method for robotic arms under payload mass uncertainty. The corresponding motion planning problem is stated as a chance-constrained nonlinear optimal control problem (NOCP) subject to kinematics and rollover stability constraints. The latter takes the form of a chance constraint that ensures a certain probability of the robot maintaining dynamic rollover stability in the presence of payload mass uncertainty. To achieve efficient solutions to the NOCP, a novel geometric bound for the stability region is derived. The novel bound is then utilized to modify the rollover-stability constraint. To showcase its benefit, comparisons between the proposed bound of probabilistic rollover stability measure and the naive noise model are provided through statistical analysis. The formulation's practicality is demonstrated through experiments with a Kinova Jaco 2 arm mounted on a free-to-roll-over platform. Results demonstrate greater robustness of the robot's motion plan to mass uncertainty and computational efficiency of the trajectory generation.**

I. Introduction

A. Background

Robotic manipulation is needed in a wide range of applications in unstructured and rough environments since many types of mobile platforms are equipped with manipulator-like cranes for working outdoors and in the field. Well-known mobile manipulator platforms include extraterrestrial exploration robots and heavy industrial machines, such as excavators, feller-bunchers, and loaders. These and other vehicles used in construction, forestry, and mining industries regularly operate on highly unstructured uneven terrain and are required to manipulate heavy loads during their operations, while the mobile base remains stationary. The aforementioned circumstances create substantial rollover risks which, aside from the potential damage to the machine and its load, also create safety concerns for the operators. The operation of a feller-buncher, which partly motivates our research, provides a relevant illustrative example: the machine is a vehicle equipped with a hydraulic crane for felling trees; it operates in forests on rough and often steep-sloped terrain. The manipulator-like crane cuts and places trees[1] in a storage location where they are bunched—a maneuver potentially creating a rollover hazard.

The focus of this paper is motion planning for payload manipulation, as required on mobile platforms like the examples just cited, which are prone to dynamic rollover instability. Our specific goal is to develop a trajectory planner which accounts for the effect of payload mass uncertainty. One obvious solution to this problem is to plan so as to guarantee stability for the full range of possible payload masses; however, we posit that this may either lead to a solution being infeasible or to unduly conservative planning. Since time efficiency of manipulation maneuvers is important for many applications, the solution proposed in this work provides a more efficient alternative.

B. Related Literature

Rollover stability of a moving or stationary machine equipped with a large-scale, powerful robotic arm can be conveniently quantified with a Zero Moment Point (ZMP) dynamic stability measure [1]. Originally introduced in [2], an early implementation of ZMP as a measure of dynamic stability for a mobile manipulator is presented in [1], and further work on mobile robots with stability constraints evolved from it. Guided by the ZMP formulation, a mobile manipulator's base generates stability-compensating motions, while the manipulator arm is executing tasks [3], [4]. By using potential functions derived from stability measures including the ZMP formulation, stability-compensating motion can also be generated for manipulator arms, as demonstrated in [5]–[10]. However, stability-compensating motions aim to complete a task while optimizing stability, while stability-constrained time-optimal motions aim to complete a task within the shortest amount of time without violating the stability constraint. The former will in general be less time-efficient than the latter. Therefore, a planning method that employs the ZMP measure as a constraint so that motions are only altered for stability compensation when rollover is imminent is worth exploring.

To address stability issues involved with mobile manipulation and navigation, some recent works [11]–[13] also showed promising results. Among all these, [13] is most

[1]Jiazhi Song and Antoine Petraki are with the Department of Mechanical Engineering, McGill University, Montreal, QC H3A 0C3, Canada. jiazhi.song@mail.mcgill.ca, antoine.petraki@mail.mcgill.ca.

[2]Brandon J. DeHart is an Adjunct Assistant Professor in the Department of Electrical and Computer Engineering and the Manager of the Waterloo RoboHub, University of Waterloo, Waterloo, ON N2L 3G1, Canada. brandon.dehart@uwaterloo.ca.

[3]Inna Sharf is a Professor at the Department of Mechanical Engineering, McGill University, Montreal, QC H3A 0C3, Canada. She is currently a Lead Researcher at FPInnovations, Pointe-Claire, QC H9R 3J9, Canada inna.sharf@mcgill.ca.

[1]https://youtu.be/fn8MZc15vcY

relevant to our work since it involves applying the ZMP constraint to the trajectory optimization of a wheeled-legged quadrupedal robot. However, since the focus of [13] is to plan the overall motion of the quadruped, to speed up the trajectory optimization component, the ZMP constraint is applied to the robot by treating it as a single rigid body supported by massless legs. Although the rigid body assumption is valid for planning overall motions when leg motions are limited, it does not apply to manipulation planning due to the heavy masses located away from a robot's body/base.

For base-stationary manipulations specifically, rollover prediction systems were developed in [14]–[16] to achieve safe truck-trailer and excavator operations. However, [14] and [15] carried *static* stability assumptions in their treatment of the rollover-avoidance issue and [16] is focused on the rollover-free modification of a human tele-operator's control input using normalized energy (NE) stability measure, without considering autonomous manipulation planning. None of the aforementioned works apply to more complex manipulation tasks where the autonomous manipulator moves fast and the loads are heavy. Hence, our work does not treat manipulator reconfigurations as static and gives special care to the *dynamic* effects of autonomous manipulation.

In the context of time-optimal rollover-free manipulation planning, the dimension reduction technique to produce a kinematically simpler, yet functionally close topology of the crane has been demonstrated to allow for online motion planning in our previous work [17]. In that work, the ZMP measure is used as a constraint for the nonlinear time-optimal control formulation of the motion planning problem. However, the ZMP stability constraint was treated in a *deterministic* way, meaning, that perfect knowledge of the manipulated payload mass is assumed. In reality, although a robot can be equipped with sensors to estimate the payload mass, the estimation may not be precise. This is especially the case in timber-harvesting operations and open-pit mining where the machines are hydraulically actuated and payloads are irregular and often too heavy for precise apparatus such as a force/torque sensor to be employed. As a result, when a robot is executing motions close to its stability limits on rough terrain, a deterministic ZMP planning formulation can generate trajectories that violate the stability constraint due to payload mass uncertainty.

To accommodate the payload mass uncertainty caused by either absence of estimation or corresponding errors, a *chance-constrained* trajectory planning formulation is explored here. Within the chance-constrained framework, we propose to implement a constraint on the *probability* of ZMP constraint violation. Several recent research works [18]–[20] in the context of autonomous driving and flight have shown the benefit of calculated risk-taking enabled by chance constraints. However, all of the aforementioned works focus on collision avoidance issues that are addressed with a different approach and are for vehicles different from those considered here. At the application level, this means that the previously demonstrated solutions [18]–[20] cannot guarantee rollover stability. From the theoretical perspective, the uncertainty models and the problem formulations in [18]–[20] cannot be applied to the ZMP-constrained planning problem as collision avoidance constraints are formulated in the Euclidean space while the ZMP measure is a function related to the robot, and the payload's kinematic states and inertial parameters. Hence, the modeling of stochastic ZMP measure has to be separately addressed.

C. About this Paper

In this paper, we consider the ZMP-stable manipulation planning on inclined terrain with the knowledge of an estimated payload mass and the distribution of that estimate. Using the distribution, a chance-constrained trajectory planning problem can be formulated. Consequently, the method will allow different robots to adjust the manipulation performance according to variables such as mass sensing accuracy, terrain steepness, actuator limits, and payload to overall mass ratio. To the best of the authors' knowledge, the proposed method is the first to address the above issues and the experiments are the first of this kind to show the real-world performance of rollover-free manipulation planning. The proposed method also has the additional benefit of being computationally efficient for online planning so new motion plans can be generated fast enough for different payload objects and arm configurations, so as not to impede the robot's speed of operation.

The structure of this paper is as follows: In Section II, a brief theoretical background will be provided for the kinematic equation of a mobile manipulator and the ZMP stability measure. In Section III, we present the trajectory planning optimal control problem (OCP) formulation along with the chance constraint. In Section IV, a geometrical transformation of the chance constraint for the ZMP measure will be introduced for improved computational efficiency. In Section V, the performance of the proposed method will be shown through a numerical demonstration and an experiment. Section VI will conclude the paper.

II. Theoretical Background

A. Simplified Kinematic Model of Mobile Manipulator

The kinematic model of a mobile platform equipped with a serial manipulator (crane) can be derived by treating it as a system of links connected by various joints, with link index $i \in \{0, 1, \cdots, n\}$, where n refers to the end-effector and payload link. The inertial and body-fixed reference frame of each link is denoted by $\mathcal{I}$ and $\mathcal{F}_i$, respectively. To achieve a fast computation speed for online planning, a dimension reduction as mentioned in [17] for the manipulator is implemented. To reduce the problem dimension, a simplified manipulator model that only involves the end-effector's angle q_1 measured about the vertical rotation axis of joint 1 (the swing joint) and distance d from that axis, along with their rates and accelerations relative to the swing axis are used. This simplification, illustrated in Figure 1, is

feasible under the condition that the full manipulator states can be recovered using a differentiable inverse kinematics equation [17]. The simplified kinematics is written in the general form:

$$\dot{\tilde{\boldsymbol{x}}} = \tilde{\boldsymbol{g}}(\tilde{\boldsymbol{x}}, \tilde{\boldsymbol{u}}), \tag{1}$$

where $\tilde{\boldsymbol{x}} = [q_1, \dot{q}_1, d, \dot{d}]^T$, and $\tilde{\boldsymbol{u}} = [u_{q_1}, u_d]$. Recalling that subscript n refers to the end-effector and payload component of the robot, the x and y components of $\boldsymbol{p}_n^{\mathcal{F}_0} - \boldsymbol{p}_b^{\mathcal{F}_0}$ which locates the end-effector relative to the base location in base frame $\mathcal{F}_0$ can be expressed as $[x_n, y_n]^T = [-d\sin q_1, d\cos q_1]^T$. Although the base is considered to be static in this paper, different base orientations can be addressed as a result of differentiating reference frames $\mathcal{I}$ and $\mathcal{F}_0$.

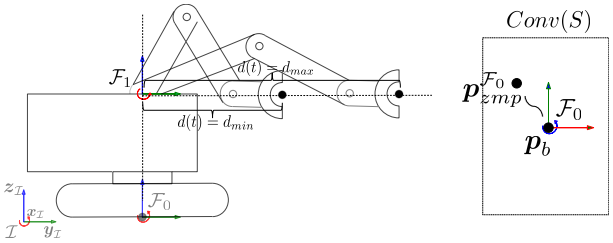

Fig. 1: Schematic diagram of a mobile manipulator reduced dimensions (left) and the support polygon (right).

In addition to the kinematics equation (1), a geometric construction called the support polygon is used in this paper. The support polygon, denoted by $Conv(S)$, is a convex hull formed by the contact points between the mobile base and the ground. The support polygon, illustrated in the right of Figure 1, is rectangular-shaped for most mobile platforms supported by tracks or four wheels.

B. ZMP Dynamic Stability Measure

The ZMP measure, originally proposed in [2], is a method designed to quantify the dynamic stability of connected rigid bodies situated on ground surface, by using their kinematics and inertial parameters. Due to the potential of the ZMP formulation to speed up computations compared to dynamics based methods, it became our method of choice.

According to [1], the location of ZMP is found based on the following equation:

$$\boldsymbol{M}_{zmp}^{\mathcal{F}_0} = \sum_{i=0}^{n} (\boldsymbol{p}_i^{\mathcal{F}_0} - \boldsymbol{p}_{zmp}^{\mathcal{F}_0}) \times m_i(\ddot{\boldsymbol{p}}_i^{\mathcal{F}_0} - \boldsymbol{g}^{\mathcal{F}_0}) \tag{2}$$

where n stands for the highest link index, $\boldsymbol{M}_{zmp}^{\mathcal{F}_0} = [0, 0, M_z]^T$, $\boldsymbol{p}_{zmp}^{\mathcal{F}_0} - \boldsymbol{p}_b^{\mathcal{F}_0} = [x_{zmp}, y_{zmp}, 0]^T$ is the ZMP location relative to the base frame, $\boldsymbol{p}_i^{\mathcal{F}_0} - \boldsymbol{p}_b^{\mathcal{F}_0} = [x_i, y_i, z_i]^T$ is each link's relative center of mass coordinates, $\ddot{\boldsymbol{p}}_i^{\mathcal{F}_0} = [\ddot{p}_{x,i}, \ddot{p}_{y,i}, \ddot{p}_{z,i}]^T$ is each link CoM's absolute acceleration in 3-D space, and $\boldsymbol{g}^{\mathcal{F}_0} = \boldsymbol{R}\boldsymbol{g}^{\mathcal{I}} = [g_x, g_y, g_z]^T$ denotes the gravitational acceleration expressed in body-fixed frame $\mathcal{F}_0$, where $\boldsymbol{R}$ is a rotation matrix that captures the orientation change between $\mathcal{I}$ and $\mathcal{F}_0$. The superscript $\mathcal{F}_0$ signifies a quantity expressed in the base-fixed frame $\mathcal{F}_0$.

Subsequently, the coordinates of the ZMP relative to the base frame are written as

$$\begin{aligned} x_{\text{zmp}} &= \frac{\sum_i m_i(\ddot{p}_{z,i} - g_z)x_i - \sum_i m_i(\ddot{p}_{x,i} - g_x)z_i}{\sum_i m_i(\ddot{p}_{z,i} - g_z)} \\ y_{\text{zmp}} &= \frac{\sum_i m_i(\ddot{p}_{z,i} - g_z)y_i - \sum_i m_i(\ddot{p}_{y,i} - g_y)z_i}{\sum_i m_i(\ddot{p}_{z,i} - g_z)}. \end{aligned} \tag{3}$$

Thus, the vehicle is dynamically stable when $\boldsymbol{p}_{\text{zmp}} \in Conv(S)$, but has the tendency to roll over otherwise. More details on (1), (2), and (3) can be found in [21] but are omitted here to allow for the main focus of this paper.

III. Chance Constrained Trajectory Planning with Simplified Kinematics

Recalling the possibility of ZMP violation caused by payload mass inaccuracy, as we discussed in Section I, the ZMP coordinates can be treated as a function of a random variable m_n that represents the payload mass, which we assume remains constant over the planning horizon. In the context of manipulation, the ZMP coordinates are also evolving with time. For a machine whose motion can be described by (1), the ZMP stability constrained trajectory planning problem with specified initial and final configurations can thus be formulated into the following nonlinear OCP (NOCP):

$$\min_{\boldsymbol{u}} \quad \int_{t_0}^{t_f} 1 \, \mathrm{d}t. \tag{4}$$

$$\text{s.t.} \quad \dot{\tilde{\boldsymbol{x}}} = \tilde{\boldsymbol{g}}(\tilde{\boldsymbol{x}}, \tilde{\boldsymbol{u}}) \quad \tilde{\boldsymbol{x}}(t_0) = \tilde{\boldsymbol{x}}_0 \quad \tilde{\boldsymbol{x}}(t_f) = \tilde{\boldsymbol{x}}_f$$

$$\underline{\tilde{\boldsymbol{x}}} \preccurlyeq \tilde{\boldsymbol{x}}(t) \preccurlyeq \overline{\tilde{\boldsymbol{x}}}, \quad \underline{\tilde{\boldsymbol{u}}} \preccurlyeq \tilde{\boldsymbol{u}}(t) \preccurlyeq \overline{\tilde{\boldsymbol{u}}}$$

$$\mathbf{Pr}\left(\boldsymbol{p}_{\text{zmp}}(m_n, t) \in Conv(S)\right) \geq \rho \;\forall\; t \in [t_0, t_f] \tag{4a}$$

where $\preccurlyeq$ is defined as vector component-wise inequality, underline $\underline{\cdot}$ and overline $\overline{\cdot}$ stand for the lower and upper bounds on a variable, respectively. The state and input constraints ensure that the machine's configuration, the corresponding rates, and accelerations are feasible. With $\mathbf{Pr}(\cdot)$ representing the probability of an event, the inequality (4a) represents the *chance* constraint expressed in probability of violating the ZMP constraint.

The real number $\rho \in (0, 1)$ is a user-specified threshold on that probability and is defined based on the risk tolerance of specific applications. It is worth noting that $\rho = 1$ is excluded in the formulation due to the analytical results, as presented in the latter part of this paper, being based on normally distributed uncertain mass. As an example, for manipulators mounted on platforms that possess self-recovering capabilities, such as the Spot[2] platform, ρ can be set to values lower than 0.95 to allow for less limiting motions since the robotic platform can recover itself from a fall without much effort. In contrast, for autonomous mobile manipulators commonly used in the timber harvesting

[2]https://www.bostondynamics.com/products/spot

industry, $\rho \geq 0.99$ is more appropriate due to the difficulty of rollover recovery.

It might be tempting for one to address the mass uncertainty issue by deriving a safety margin for the ZMP constraint based on the payload mass extrema. However, this is likely to become a conservative and thus self-limiting margin that results in the robot not being able to manipulate a payload even when it is safe to do so. Additionally, a chance constraint framework employed here is more general in the sense that it can be easily modified to accommodate a scenario where the user would like to guarantee 100% success based on payload mass extremum information, as the extremum can be treated as a finite-sized 100% probability bound, while the reverse cannot be said.

As pointed out in [17], solving the ZMP constrained NOCP for simplified kinematics as defined in (4) also guarantees the dynamic stability of the real robot with full kinematics since the ZMP constraint in (4) is calculated from the full kinematics, mapped from the simplified one. Therefore, the chance-constrained formulation (4) can maintain the probability of ZMP-stable condition for the real robot above threshold ρ at any time instant t along the trajectory. It is worth noting that, as mentioned in [22], the now added nonlinear chance constraint (4a) results in (4) being numerically inefficient to solve as its gradient can only be evaluated numerically at every computational iteration. Therefore, a geometric interpretation of (4a) is required to reduce the numerical complexity added by the chance constraint.

IV. Geometric Interpretation of Chance-constrained ZMP

For many manipulators used to relocate heavy payloads, such as the articulated machines used in forestry, the main component of most pick-and-place motions is sideways or lateral load transportation. It is on these types of motions that we focus the theoretical development in this section. The measured payload mass $\bar{m}_n$ is also assumed to be normally distributed around the actual mass m_n with reasonable error. Consequently, the derivation of the chance constraint is based on the following assumptions:

Assumption 1. *The accelerations of the robot's links in the base-fixed $\boldsymbol{z}_0$ direction and the extend/retract velocity and acceleration, $\dot{d}$ and $\ddot{d}$, are negligible when executing lateral movements.*

Assumption 2. *The measured payload mass follows a normal distribution $\bar{m}_n \sim \mathcal{N}\left(m_n, \sigma^2\right)$ where $\sigma \ll \Sigma_i m_i$.*

A. Chance-constrained ZMP Bound

With Assumption 1, the ZMP coordinates (3) can be written as:

$$\begin{aligned} x_{\text{zmp}} &= \frac{\sum_i m_i g_z x_i - \sum_i m_i g_x z_i + \sum_i m_i \ddot{p}_{x,i} z_i}{\sum_i m_i g_z} \\ y_{\text{zmp}} &= \frac{\sum_i m_i g_z y_i - \sum_i m_i g_y z_i + \sum_i m_i \ddot{p}_{y,i} z_i}{\sum_i m_i g_z}. \end{aligned} \tag{5}$$

Defining $[x_c, y_c, z_c]^T = \boldsymbol{p}_c^{\mathcal{F}_0} - \boldsymbol{p}_b^{\mathcal{F}_0} = \frac{\sum_{i=0}^n m_i (\boldsymbol{p}_i^{\mathcal{F}_0} - \boldsymbol{p}_b^{\mathcal{F}_0})}{\sum_{i=0}^n m_i}$ as the center of mass location of the whole robot including payload in $\mathcal{F}_0$, (5) can be represented as

$$\begin{aligned} x_{\text{zmp}} &= x_c - \frac{g_x}{g_z} z_c + \frac{\sum_i m_i \ddot{p}_{x,i} z_i}{\sum_i m_i g_z} \\ y_{\text{zmp}} &= y_c - \frac{g_y}{g_z} z_c + \frac{\sum_i m_i \ddot{p}_{y,i} z_i}{\sum_i m_i g_z}, \end{aligned} \tag{6}$$

which can be re-arranged into the following form:

$$\begin{bmatrix} x_{\text{zmp}} \\ y_{\text{zmp}} \end{bmatrix} = \underbrace{\begin{bmatrix} 1 & 0 & -\frac{g_x}{g_z} \\ 0 & 1 & -\frac{g_y}{g_z} \end{bmatrix}}_{\boldsymbol{P}} (\boldsymbol{p}_c^{\mathcal{F}_0} - \boldsymbol{p}_b^{\mathcal{F}_0}) + \frac{1}{g_z} \begin{bmatrix} \sum_i \frac{m_i \ddot{p}_{x,i} z_i}{M} \\ \sum_i \frac{m_i \ddot{p}_{y,i} z_i}{M} \end{bmatrix}, \tag{7}$$

where $M = \sum_i m_i$ is the total mass including the payload mass. The division by g_z in (7) is valid as long as $g_z \neq 0$, which holds for ground vehicles where $g_z < 0$ is guaranteed by definition.

Denoting variables associated with the measured payload mass with $\bar{\cdot}$ and error terms with $\tilde{\cdot}$, the difference between the actual ZMP coordinates (7) and the nominal ZMP can be expressed as:

$$\begin{aligned} \tilde{\boldsymbol{p}} &= \boldsymbol{p}_{\text{zmp}} - \bar{\boldsymbol{p}}_{\text{zmp}} \\ &= \boldsymbol{P} \tilde{\boldsymbol{p}}_c + \frac{1}{g_z} \begin{bmatrix} \sum_i \frac{m_i \ddot{p}_{x,i} z_i}{M} - \sum_i \frac{\bar{m}_i \ddot{p}_{x,i} z_i}{\bar{M}} \\ \sum_i \frac{m_i \ddot{p}_{y,i} z_i}{M} - \sum_i \frac{\bar{m}_i \ddot{p}_{y,i} z_i}{\bar{M}} \end{bmatrix}, \end{aligned} \tag{8}$$

where $\tilde{\boldsymbol{p}}_c = \boldsymbol{p}_c^{\mathcal{F}_0} - \bar{\boldsymbol{p}}_c^{\mathcal{F}_0}$ is the difference between the actual center of mass position and the estimated one. Under Assumption 2, (8) can be further simplified to

$$\tilde{\boldsymbol{p}}(\tilde{m}_n) \approx \frac{\tilde{m}_n}{M} \boldsymbol{P} (\boldsymbol{p}_n^{\mathcal{F}_0} - \boldsymbol{p}_b^{\mathcal{F}_0}) + \frac{\tilde{m}_n z_n}{M g_z} \begin{bmatrix} \ddot{p}_{x,n} \\ \ddot{p}_{y,n} \end{bmatrix}, \tag{9}$$

where $\tilde{m}_n = m_n - \bar{m}_n$. A bound on the ZMP estimation error can be derived based on triangle inequality from (9), using the Euclidean norm $\| \cdot \|$:

$$\begin{aligned} \|\tilde{\boldsymbol{p}}(\tilde{m}_n)\| \leq \frac{|\tilde{m}_n|}{M} &\max\left(\left\| \boldsymbol{P} (\boldsymbol{p}_n^{\mathcal{F}_0} - \boldsymbol{p}_b^{\mathcal{F}_0}) \right\| \right) \\ &+ \left| \frac{\tilde{m}_n z_n}{g_z M} \right| \max\left(\left\| \begin{bmatrix} \ddot{p}_{x,n} \\ \ddot{p}_{y,n} \end{bmatrix} \right\| \right). \end{aligned} \tag{10}$$

Since $g_z < 0$, and $\boldsymbol{P}(\boldsymbol{p}_n^{\mathcal{F}_0} - \boldsymbol{p}_b^{\mathcal{F}_0})$ represents m_n's center of mass location projected along the vertical direction onto the support polygon, $\max\left(\left\| \boldsymbol{P} (\boldsymbol{p}_n^{\mathcal{F}_0} - \boldsymbol{p}_b^{\mathcal{F}_0}) \right\| \right)$ is achieved when the end-effector is fully extended and $[x_n, y_n]^T$ points in the same direction as the terrain gradient represented in $\mathcal{F}_0$. Therefore, the newly defined $h_{s,max} = \frac{\max\left(\left\| \boldsymbol{P} (\boldsymbol{p}_n^{\mathcal{F}_0} - \boldsymbol{p}_b^{\mathcal{F}_0}) \right\| \right)}{M}$ can be found based on the orientation of the base. By taking the second order derivative of $\boldsymbol{p}_n^{\mathcal{F}_0}$ defined in Section II-A with respect to time and neglecting the $\dot{d}$ and $\ddot{d}$ terms, we arrive at:

$$\begin{bmatrix} \ddot{p}_{x,n} \\ \ddot{p}_{y,n} \end{bmatrix} = \begin{bmatrix} d \sin q_1 \dot{q}_1^2 - d \cos q_1 \ddot{q}_1 \\ -d \cos q_1 \dot{q}_1^2 - d \sin q_1 \ddot{q}_1 \end{bmatrix}, \tag{11}$$

and taking the max 2-norm of (11), we obtain

$$a_{n,max} = \max\left(\left\|\begin{bmatrix}\ddot{p}_{x,n}\\ \ddot{p}_{y,n}\end{bmatrix}\right\|\right) = \sqrt{d_{max}^2 \dot{q}_{1,max}^4 + d_{max}^2 \ddot{q}_{1,max}^2}. \tag{12}$$

Since

$$\left|\frac{\tilde{m}_n z_n}{g_z M}\right| a_{n,max} \leq \frac{z_n}{-g_z M} a_{n,max} |\tilde{m}_n|,$$

by defining $h_{d,max} = \frac{z_n}{g_z M} a_{n,max}$, and $\tau = h_{s,max} + h_{d,max}$, we arrive at:

$$\|\tilde{\boldsymbol{p}}(\tilde{m}_n)\| \leq \tau |\tilde{m}_n|, \tag{13}$$

where $\tau|\tilde{m}_n|$ is a function of the robot's orientation, configuration limits, angular rate and acceleration limits, inertial parameters, and mass uncertainty.

Define $\Gamma(\gamma)$ as a closed set $[0, \gamma]$ where $\gamma \in \mathbb{R}^+$. Since the magnitude of $\|\tilde{\boldsymbol{p}}(\tilde{m}_n)\|$ is bounded by $\tau|\tilde{m}_n|$ as derived in (13), we further arrive at:

$$\mathbf{Pr}(\|\tilde{\boldsymbol{p}}(\tilde{m}_n)\| \in \Gamma(\gamma)) \geq \mathbf{Pr}(\tau|\tilde{m}_n| \in \Gamma(\gamma)), \tag{14}$$

and hence $\mathbf{Pr}(\|\tilde{\boldsymbol{p}}(\tilde{m}_n)\| \in \Gamma(\gamma)) \geq \rho$ is guaranteed for any probability threshold ρ when $\mathbf{Pr}(\tau|\tilde{m}_n| \in \Gamma(\gamma)) \geq \rho$. Since $\mathbf{Pr}(\tau|\tilde{m}_n| \in \Gamma(\gamma)) = \mathbf{Pr}(\tau\tilde{m}_n \in [-\gamma, \gamma])$ and, under Assumption 2, $\tau\tilde{m}_n \sim \mathcal{N}\left(0, \tau^2\sigma^2\right)$, it is straightforward to find the chance-constrained ZMP bound

$$\gamma : \mathbf{Pr}\left(\tau|\tilde{m}_n| \in \Gamma\left(\gamma\right)\right) \geq \rho. \tag{15}$$

Geometrically, the inequality (15) can be interpreted as: the chance of the ZMP being located within a distance γ away from the nominal ZMP is greater than ρ. It is worth noting that since the magnitude of γ is linear with respect to $\tilde{m}_n$, the derivation of γ provided in this paper can easily be extended to other non-normal statistical distributions of $\tilde{m}_n$, as long as the distribution has defined probability bounds.

B. Chance-constrained Rollover Avoidance

As illustrated by the inequality (14) in Section IV-A, once γ has been determined from (15), the following inequality:

$$\mathbf{Pr}(\|\tilde{\boldsymbol{p}}(\tilde{m}_n)\| \in \Gamma(\gamma)) \geq \rho \tag{16}$$

is guaranteed. Intuitively, inequality (16) shows that more than ρ of the ZMP distribution can be bounded within a circle with center $\bar{\boldsymbol{p}}_{\text{zmp}}$ and radius γ denoted by $\mathcal{O}(\bar{\boldsymbol{p}}_{\text{zmp}}, \gamma)$. Therefore, the chance constraint (4a) can be replaced by bounding the circle within the support polygon:

$$\mathcal{O}(\bar{\boldsymbol{p}}_{\text{zmp}}(t), \gamma) \in Conv(S) \ \forall \ t \in [t_0, t_f]. \tag{17}$$

The new constraint (17) is equivalent to constraining the ZMP to stay within a smaller support polygon $Conv(S)^-$ that is geometrically similar to $Conv(S)$, whereby each new edge is a distance γ closer to the interior from its original position.

It is worth noting that since the variable γ of the circle $\mathcal{O}(\bar{\boldsymbol{p}}_{\text{zmp}}, \gamma)$ is derived from (13), it takes into account multiple factors, including the chance constraint threshold ρ and robot properties. Specifically, $h_{s,max}|\tilde{m}_n|$ is a function of static factors including the ratio between mass estimation uncertainty and overall mass of the robot, the coordinates in space of the uncertain mass, and the robot's orientation; $h_{d,max}|\tilde{m}_n|$ is a function of most static factors along with dynamic factors, including maximum joint rates and joint accelerations in the form of maximum acceleration of the uncertain mass. As a result, the robot's motion can adapt to different scenarios and can appear more "aggressive" when the parameters are in favor of stability while less so otherwise. This behavior can be observed from the simulations and experiments presented in the following Sections V and VI.

V. Simulation Results

To help illustrate how the chance-constrained formulation can deal with payload mass uncertainty, we begin by presenting simulation results in this section. For the simulations, a 6-DoF Kinova Jaco 2 arm[3] in Figure 2 mounted on a free-to-roll-over platform will be the robot of choice.

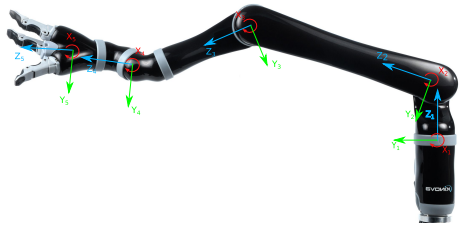

Fig. 2: Joint axes definition of the Kinova Jaco 2 arm.

A. Manipulator Platform Parameters

In order to emulate the motion of articulated machines such as feller-bunchers and excavators, the fourth joint of the Jaco arm is kept unchanged and hence only 5 DoFs of the arm are utilized. Details of the inertial parameters of the Jaco 2 can be found online[4]. The arm's joint angular rate (rad/s) and acceleration (rad/s^2) limits are:

$$\begin{aligned} -0.55 \leq \dot{q}_1 \leq 0.55, \quad -\pi/2 \leq \ddot{q}_1 \leq \pi/2 \\ -0.45 \leq \dot{q}_{2-5} \leq 0.45, \quad -\pi/2 \leq \ddot{q}_{2-5} \leq \pi/2. \end{aligned} \tag{18}$$

The Jaco 2 arm is mounted onto a free-to-roll-over plate-like base with dimensions of 40x50x5 cm and with a mass of 2.271 kg. The base is designed to allow the robot to roll over during most operations. Rollover is especially likely to happen when the arm has a payload in its end-effector. Three objects: a roll of tape, a wrench, and a weight will appear in various tests. The masses of the tape and wrench are 0.370 kg and 0.677 kg, respectively. The payload named "1 kg" is the cylindrical weight with a mass of 1 kg.

[3]https://assistive.kinovarobotics.com/product/jaco-robotic-arm
[4]https://github.com/Kinovarobotics/kinova-ros

B. Statistical Analysis

To demonstrate the properties of the proposed chance constraint formulation (17), the ZMP distribution of the robot is found by solving (3) of the robot's full kinematics with payload masses randomly sampled from a normal distribution with mean equal to the estimated mass. The distribution of the payload mass follows $\sim \mathcal{N}(0.370, \sigma^2)$, where the mean 0.370 kg corresponds to the mass of a roll of tape. Four scenarios that consist of 5000 mass samples each are considered. Each scenario is defined by a set of parameters shown in Table I that includes a pitch angle θ (nose up corresponds to positive pitch) of the robot base resulting from terrain surface unevenness, and an assumed payload mass standard deviation. The proposed bounding circle is then found for each scenario so its coverage rate of the ZMP distribution can be shown.

To demonstrate the effectiveness of the proposed bound when a robot's configuration changes, for all scenarios except scenario 2, q_1 is sampled uniformly from $[0, 2\pi]$. For scenario 2, q_1 is sampled uniformly from the range $[-\frac{1}{8}\pi, \frac{1}{8}\pi]$ to show the coverage rate near worst-case configuration. The worst-case configuration exists in scenario 2 due to the non-zero terrain surface angle ($\theta = -30°$) . In scenario 4, an extra mass is assigned to the robot's base so the impact on the proposed bound γ due to a robot's mass change can be illustrated. In all four scenarios, maximum joint velocity and acceleration are prescribed to joint q_1 to showcase the performance of the method for dynamic motions.

As a comparison to the proposed circular bound, a naive constraint circle, referred to as the "naive circle" in the following, is employed. For normally distributed payload mass, the naive circle is a circular bound that covers the threshold probability of the ZMP distribution for the robot on a horizontal terrain surface. Due to the lack of an existing formulation, the naive circle is generated without considering the effect of changes in the robot's mass. Both the naive and proposed chance-constrained circles are constructed to bound 2σ ($\rho \approx 0.95$) of the dynamic ZMP distribution. For the simulation results to stay consistent with the analysis provided in Section IV, -2σ can result in uncertain payload mass becoming negative. This, however, does not cause any problems since the impact of this negative mass on ZMP location is similar to total mass reduction of the robotic arm: it brings the ZMP further inside $Conv(S)$ and is of less importance compared to the $+2\sigma$ extremum.

Scenario	θ (deg.)	σ	Extra mass (kg)	γ (cm)
1	0	0.4	0	4.74
2	-30	0.4	0	6.64
3	0	0.5	0	5.93
4	0	0.4	3	3.63

TABLE I: Four scenarios considered in the statistical analysis, their associated parameters, and bound radius γ.

The statistical analysis results for the aforementioned scenarios are shown in Figure 3, where (3a)-(3d) correspond, respectively, to scenarios 1-4. Figure (3a) shows that the proposed circular bound derivation based on τ of (13) has the same coverage rate as the naive circular bound on flat ground with a specific robot overall mass. However, Figure (3b) shows that when the terrain becomes steeper in Scenario 2, the naive circle can no longer bound 2σ of the distribution while the proposed circular bound increases in size so more than the specified 95% of the distribution is bounded.

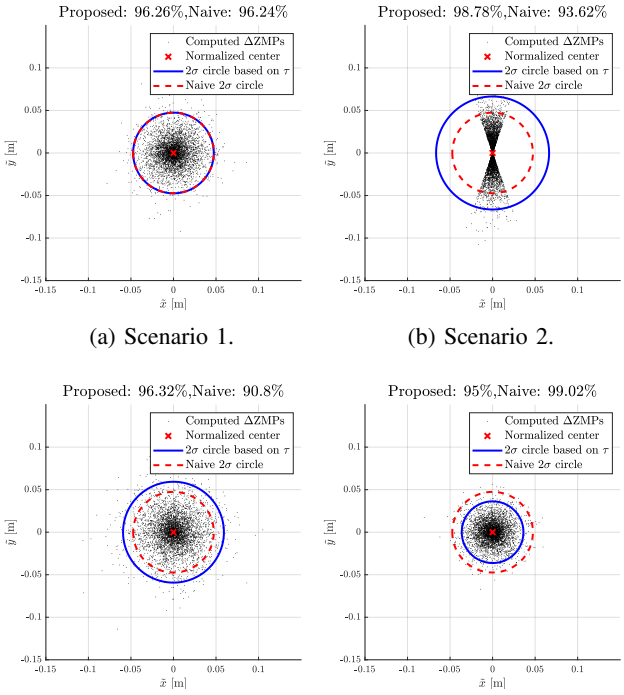

(a) Scenario 1. (b) Scenario 2.

(c) Scenario 3. (d) Scenario 4.

Fig. 3: Simulated ZMP estimation error to showcase the benefit of the proposed ZMP margining method over a naive method. The sample coverage rates are presented in the title of each plot. Since the joint angle of the robot is also sampled randomly, the ZMPs are normalized by taking the difference between each sampled ZMP and the nominal ZMP that corresponds to its configuration. Therefore, sampled ΔZMPs are shown in each plot along with the normalized center with coordinate $[0, 0]^T$.

For cases where the estimation accuracy of payload mass is lowered to $\sigma = 0.5$ kg in Scenario 3, Figure (3c) shows that the naive circle fails to contain the specified distribution while the proposed circular bound is capable of expanding and covering the right amount. Finally, Figure (3d) shows that as the overall mass of the robot increases in Scenario 4, the proposed circular bound shrinks so that it does not over-constrain the problem as much as the naive circle. The bound γ of each scenario is presented in Table I. Overall, compared to a constant bound, the proposed bound shrinks its size when the parameters result in tighter ZMP distribution for better motion feasibility, while it increases its size otherwise to ensure an adequate safety assurance.

C. Chance-constrained vs. Conservative Margin Success Rate Comparison

To demonstrate the *benefit* of chance constraint on increasing motion planning feasibility over a constant safety margin, another set of randomized simulations is generated for different cases. Solutions of the NOCP in (4) are obtained with the general optimal control solver GPOPS [23] using the Interior Point OPTimizer (IPOPT) [24] method under MATLAB environment on a Windows desktop with Intel Core i7-4770 3.40 GHz processor. The GPOPS solver is chosen for its ability to accommodate general nonlinear formulations.

A total of four cases are considered: a deterministic case with no uncertainty named 'baseline'; a non-deterministic case with a chance constraint of $\rho = 0.95$ ($\approx 2\sigma$) named '95%'; a non-deterministic case with a chance constraint of $\rho = 0.99$ ($\approx 3\sigma$) named '99%'; and, lastly, a conservatively bounded example with a constant bound of $\gamma = 8.92$ cm which corresponds to the bound of 99% chance constraint on a 30-degree slope, named 'Conservative' is used as a comparison. For all non-deterministic cases, the standard deviation is chosen to be $\sigma = 0.4$. For each set of test parameters, a total of 1000 motion plans are generated with uniformly randomly sampled manipulator states: $q_1(t_0) \in [-\pi, \pi]$, $q_1(t_f) \in [-\pi, \pi]$, $d(t_0) = d(t_f) \in [d_{min}, d_{min} + \frac{1}{2}(d_{max} - d_{min})]$, and $\theta \in [-30, 30]$.

Scenario	σ	γ_{min} (cm)	γ_{max} (cm)	Normalized success rate
Baseline	0	0	0	1
95%	0.4	2.15	5.95	0.89
99%	0.4	3.23	8.92	0.64
Conservative	0.4	8.92	8.92	0.35

TABLE II: Four scenarios considered in the planning success rate comparison, their associated mass measurement σ, minimum and maximum bound radii, and normalized success rates.

For all planning attempts, a motion plan is deemed successful only when the nonlinear programming solver arrives at a result that satisfies optimality conditions. Due to the randomized fashion of this test, some tests of the 'Baseline' scenario also encounter infeasible configurations that result in unsuccessful plans. For presentation clarity, all success rates are normalized with respect to that of 'Baseline'. It can be observed from Table II that, as expected, using a chance constraint of $\rho = 0.99$ results in a consistently larger γ and lower motion planning success rate compared to $\rho = 0.95$.

Further, using a fixed safety margin based on the "Conservative" scenario results in almost *half* of the success rate compared to the '99%' chance-constrained scenario, due to the bound size being constant in the "Conservative" case. This shows that, although a conservative fixed safety margin is capable of *guaranteeing* safety by using a worst-case assumption, doing so drastically reduces the manipulator's motion capabilities. The results of this demonstration show the benefit of the proposed bound being dependent on the manipulator's states, which in turn yields higher motion planning success rates.

VI. Experiments with Kinova Jaco 2 Arm

A. Experimental Setup

To physically demonstrate the capabilities of the proposed ZMP bounding method under dynamic motion, experiments were conducted with the same setup as mentioned in Section V-A, where the Jaco 2 arm is mounted on top of a free-to-roll-over base as shown in Figure 4.

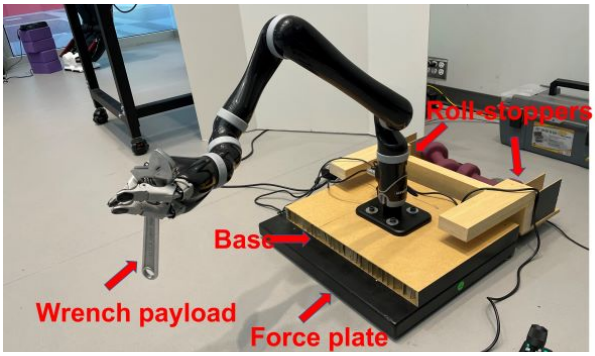

Fig. 4: Experimental setup to measure ZMP locus for comparison with planned ZMP locus.

In Figure 4, two wooden sections –"roll-stoppers"– above the robot's base are placed along one side of the base to prevent damage to the robot by stopping rollovers partway (when they occur). For the first set of experiments presented in Section VI-B to verify the predicted ZMP locations, the robot was placed on a force plate that provides measurements of ZMP location during arm motion. In Figure 4, the robot can be seen manipulating the 'wrench' payload as introduced in Section V-A. For the second set of experiments discussed in Section VI-C, solutions of NOCP in (4) are again obtained with the general optimal control solver GPOPS [23] under MATLAB environment on a Windows desktop with Intel Core i7-4770 3.40 GHz processor. The number of control points specified to GPOPS for generating the motion plans for the experiments is 40, giving an average control interval of 0.17 s. Although the solution obtained with GPOPS ensures satisfaction of constraints at control points only, given the speed of the robot, we expect the constraints to also be satisfied in-between the control points, with the robot maintaining stability throughout the full maneuver when the optimal soluton is found.

B. ZMP Verification with Force Plate

To verify that the Jaco arm is capable of following the planned trajectory and that the real ZMP trajectory is in good correspondence with the planned one, an experiment was carried out by placing the mobile manipulator structure on top of a Bertec 5060 force plate[5]. The force plate is

[5]https://www.bertec.com/products/force-plates

specifically designed for measuring the center of pressure (CoP). By definition, the CoP is equivalent to the ZMP when the ZMP is located within the support polygon. In cases where the ZMP travels outside of the support polygon, the ZMP becomes the "Imaginary-ZMP" as defined in [25]. Then, the CoP will "glide" along the support polygon when roll motion begins to occur, and violent CoP oscillations can be observed when the roll motion is stopped by the robot's base reacquiring full contact with the ground.

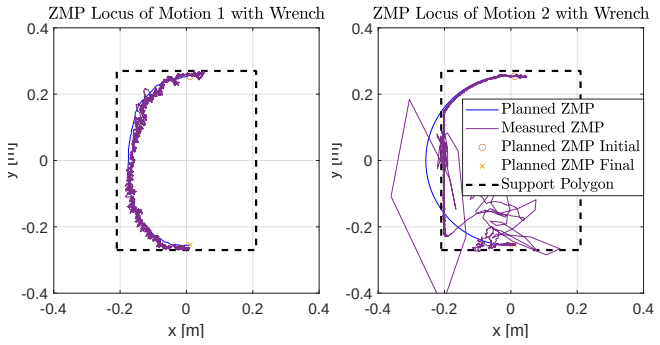

(a) ZMP loci of Motion 1. (b) ZMP loci of Motion 2.

Fig. 5: ZMP loci comparison between the planned vs. experimental for motions 1 and 2.

To conduct the verification, two motions were executed. Both motions were planned by using the actual payload mass to demonstrate planned and measured ZMP agreement. Aside from following the previously mentioned joint rate and acceleration limits (18), both Motion 1 and 2 require the arm to move between stationary initial and final configurations $\boldsymbol{q}(t_0) = [0, -1.30, -0.54, 0.27, 0]^T$ rad and $\boldsymbol{q}(t_f) = [\pi, -1.30, -0.54, 0.27, 0]^T$ rad in the shortest amount of time, with the wrench payload. However, the planning of Motion 1 follows the *deterministic* version of the ZMP-constrained NOCP formulation (4), while Motion 2 is planned based on "bang-bang" control so it is time optimal but is not constrained by ZMP stability.

The results of the verification are shown in Figure 5 for the two motions. Figure (5a) shows that, when a motion is planned based on the ZMP constraint, the planned and experimental ZMP loci agree with each other and stay within the support polygon. Figure (5b) shows that, when a motion is not planned under the ZMP constraint, a mobile robot can roll over. The rollover is characterized by the planned and experimental ZMP leaving the support polygon. The large oscillation of the experimental ZMP locus is caused by the rolled robot being caught by the "roll-stopper" and rocking back and forth before it stabilizes. The ZMP locus of Motion 2 is smoother compared to Motion 1 prior to the rollover because only joint q_1 is involved in the motion. The computation time for Motion 1 is 1.89 s while Motion 2 has an analytical solution so its computation time is negligible. It can also be observed from Figure (5b) that the planned and experimental ZMP loci agreed with each other before they left the support polygon and they also left the support polygon at the same location.

C. Manipulation Planning with Payload Mass Uncertainty

To test the effectiveness of the proposed chance-constrained formulation for increasing the robustness of the planned motion's dynamic stability to payload mass uncertainty, an experiment is designed for the experimental platform introduced in Section VI. Using the proposed chance-constrained formulation (4) with the new constraint (17), the following experimental scenario is considered: the manipulator picks up one of the three objects–tape, wrench, 1 kg cylindrical weight– but due to sensor or model inaccuracies, the payload mass is estimated to always be that of the tape (0.370 kg). A total of eight tests are carried out with the aforementioned objects, robot base roll angles (positive roll corresponds to away from the direction of "roll stopper"), and assumed standard deviations for the payload mass. All initial and final configurations of the arm are the same as those of Section VI-B. The test parameters are presented in Table III along with the stability outcome, total motion time t_f, safety margin γ computed from (15), and computation time t_c. The chance constraint threshold for all tests is set to $\rho \approx 0.95$.

	Parameters			Outcome			
Test #	Payload	Base Roll (deg.)	σ (kg)	Stable? (✓/✗)	t_f (s)	γ (cm)	t_c (s)
1	Tape	0	0	✓	6.1	0	1.77
2	Wrench	0	0	✗	6.1	0	1.77
3	Wrench	0	0.2	✓	6.1	2.66	2.19
4	Tape	12	0.2	✓	8.9	2.68	3.55
5	Wrench	12	0.2	✓	8.9	2.68	3.55
6	Tape	0	0.4	✓	6.1	4.74	1.99
7	Wrench	0	0.4	✓	6.1	4.74	1.99
8	1 kg	0	0.4	✓	6.1	4.74	1.99

TABLE III: Test parameters and motion outcome of eight experimental tests.

A comparison between the stability outcome of Tests 1 and 2 shows that when uncertainty is not considered, rollover occurs due to the actual payload being heavier than the measurement. However, if uncertainty is considered and the proposed method is implemented as in Test 3 onward, the robot maintains its stability over the full maneuver, as indeed is the case for all stable tests indicated in Table III. Moreover, the motion execution time is unchanged between Tests 2 and 3. The stability outcomes of Tests 4 and 5 show that the proposed method can take terrain surface angle into account so that when the robot is banked unfavorably towards its side, a rollover-free motion can still be planned, albeit, with the result more conservative and taking more time to complete. Even though the ZMP measure (2) itself accommodates different base orientations, it is worth noting that the proposed bound γ in (15) also changes as the bank angle increases, since the ZMP *uncertainty* changes with robot orientation as well. Consequently, γ of Test 3 is 2.66 cm while γ of Tests 4 and 5 increases slightly to 2.68 cm.

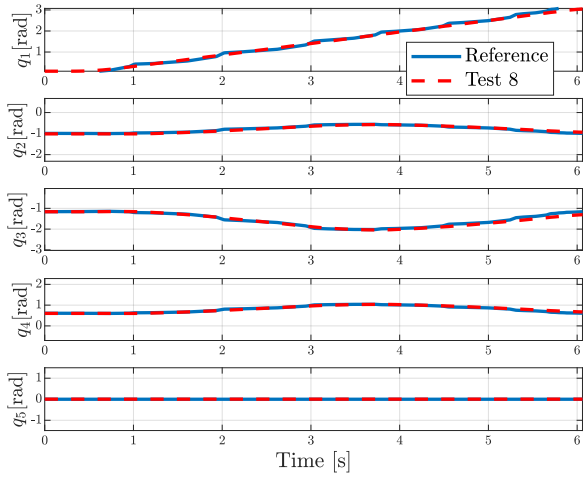

Fig. 6: Joint angles comparison of the reference and actual trajectory of Test 8.

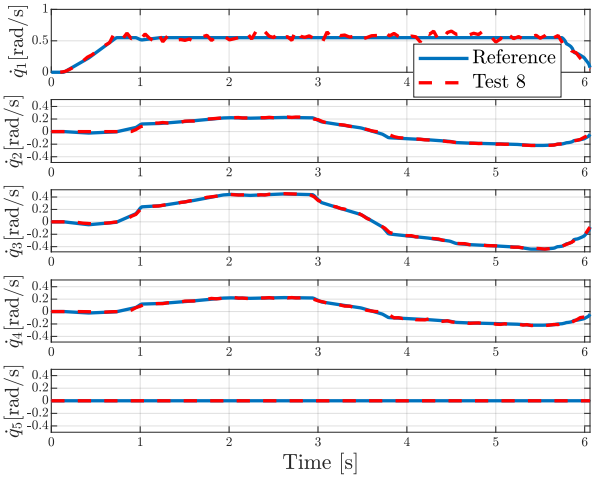

Fig. 7: Joint angular rates comparison of the reference and actual trajectory of Test 8.

Motions in Tests 6, 7, and 8 show that when a robot's mass sensing has higher uncertainty σ, a larger mass deviation can be accommodated as a result of the bound γ increasing to 4.74 cm. This is illustrated especially with Test 8, in which a motion is planned for a measured mass of 0.370 kg with $\sigma = 0.4$. Consequently, even when the actual payload mass is 1 kg, the planned motion is still dynamically stable. A comparison between the joint angles and rates of the planned motion (Reference) and the actual motions of Test 8 are shown in Figures 6 and 7. It can be observed that despite the arm using its built-in controller, the reference motion is tracked closely for all test cases. This is due to the NOCP formulation (4) accommodating the joint kinematic limits.

In Figure 8, the actual ZMP locus of the arm with the 1kg weight is shown along with the planned ZMP based on the tape's mass and the ZMP region bounded by the ZMP loci found by modifying the tape's mass by $\pm 2\sigma$, in this case, ± 0.8 kg. We observe that the outer edge of the

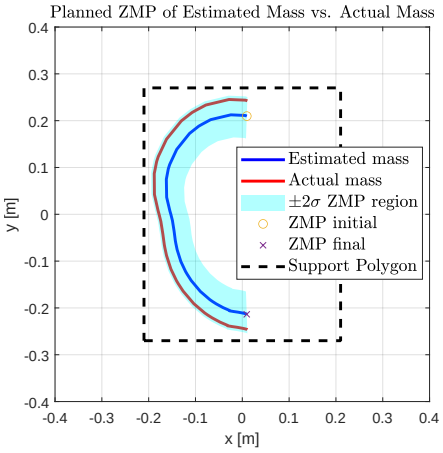

Fig. 8: Test 8 with the planned ZMP loci based on the estimated mass (tape), the actual mass (1 kg), and confidence interval for $\pm 2\sigma$ of the estimated mass.

bounded region approaches the edge of the support polygon during motion, and also the region's width does not vary significantly. Based on this, we suggest that the derived bound γ (4.74 cm in Test 8) resembles the actual deviation of the ZMP loci when the payload's mass, 1kg, is near the limit of the assumed inaccuracy at 1.17kg.

Motion snapshots of Tests 1, 2, 3, 5, and 8 are presented in Figure 9 (column-wise). For each test, snapshots of the initial pose (top), intermediate pose (middle), and halfway pose (bottom) are included. Halfway poses are chosen because that is when the ZMP is most likely to travel outside of the support polygon as the arm is configured parallel to the short edges of the support polygon. The second half of the test motions is omitted for brevity. It can be observed from the halfway (bottom snapshots) poses of Tests 1, 3, and 8 that the arm tends to retract the end-effector as σ increases. This shows that the proposed method allows the robot to adapt its motions to different mass uncertainty levels. Moreover, although end-effector retraction occurs, due to the scale of retraction being small with respect to the lateral motion, Assumption 1 did hold and the analytical results provided in Section IV remained valid. From the snapshots of Test 2 in Figure (9b), robot rollover can be observed in the halfway pose at timestamp $t = 2.9$ s. It is worth noting that, Tests 1, 2, 3, 6, 7 and 8 demonstrate the same value of t_f with different σ values. This is due to the time-optimal algorithm being capable of finding a trajectory that allows Joint 1 to maintain maximum angular rate, while having the arm retract its end-effector further when σ is high. Longer t_f solely due to higher σ can be expected on manipulators that have lower maximum end-effector retraction speed.

VII. Conclusions and Discussions

To address the payload mass uncertainties that may be encountered in mobile robot manipulations, a novel chance-constrained manipulation planning formulation and

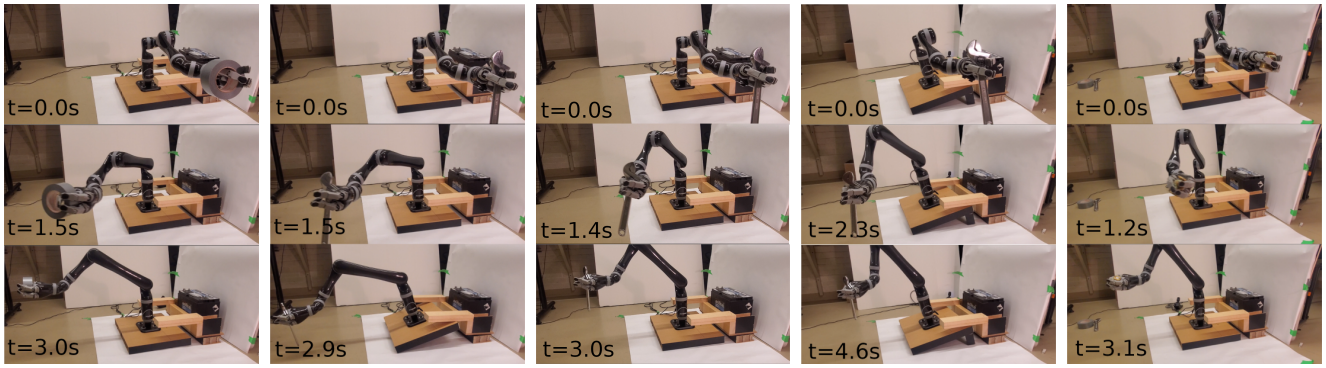

(a) Test 1. (b) Test 2. (c) Test 3. (d) Test 5. (e) Test 8.

Fig. 9: Snapshots of test motions 1, 2, 3, 5, and 8. Rollover is visible in (b) Test 2. In (d) Test 5, the base remains at the specified ground angle and is not in contact with the roll-stoppers.

its derivation are presented. Statistical analysis with a simulated Jaco 2 arm is carried out to validate the proposed geometric interpretation of the ZMP chance constraint. Experimental tests are then performed with physical Jaco 2 arm mounted on a free-to-roll-over base. Experimental results show the proposed chance-constrained bound can address the mass uncertainty issue based on different parameters such as mass uncertainty, robot attitude, and required chance of success. The ability of the chance-constrained bound to adapt to different parameters allows the motion planner to tighten and loosen the dynamic stability constraint accordingly, depending on the robot's parameters and application. The comparisons between the proposed method and conservative safety margins show that the chance-constrained bound allows for a higher planning success rate. The tests also show that the proposed bound allows the NOCP formulation to be solved fast enough for online planning.

Limitations of the proposed method stem from the model simplification and assumptions made in carrying out the mathematical analysis. Despite the geometric interpretation (17) bringing practicality to the previously numerically inefficient nonlinear chance constraint (4a), it is worth noting that it is inherently more conservative than (4a). Although this paper is focused on horizontal motions, the assumptions and analysis provided in this paper can be analogously applied to separately address vertical motions. For future research, a more general formulation that relies on less restrictive assumptions and considers uncertainty in the center of mass location of the manipulated object can be explored. The formulation can also be extended to encompass other applications where motion planning with payload mass uncertainty, such as humanoids and systems with slung loads, is of relevance.

Acknowledgement

The authors would like to thank the RoboHub at the University of Waterloo for providing the equipment and technical support for gathering experimental data. This work was supported by the National Sciences and Engineering Research Council (NSERC) Canadian Robotics Network (NCRN), the McGill Engineering Doctoral Awards and Summer Undergraduate Research in Engineering (SURE) programs.

References

[1] S. Sugano, Q. Huang, and I. Kato. Stability criteria in controlling mobile robotic systems. In *Proceedings of the 1993 IEEE/RSJ International Conference on Intelligent Robots and Systems*, pages 832–838, Yokohama, Japan, July 1993. IEEE.

[2] M. Vukobratovic and J. Stepanenko. On the stability of anthropomorphic sytems. *Mathematical Biosciences*, 15:1–37, 1972.

[3] Q. Huang, K. Tanie, and S. Sugano. Coordinated motion planning for a mobile manipulator considering stability and manipulation. *The International Journal of Robotics Research*, 19(8):732–742, 2000.

[4] K. M. E. Dine, J. Corrales-Ramon, Y. Mezouar, and J. Fauroux. A unified mobile manipulator control for online tip-over avoidance based on zmp disturbance observer. In *2018 IEEE International Conference on Robotics and Biomimetics*, pages 1437–1443, Kuala Lumpur, Malaysia, Decemner 2018. IEEE.

[5] J. Kim, W. K. Chung, Y. Youm, and B. H. Lee. Real-time zmp compensation method using null motion for mobile manipulators. In *2002 IEEE International Conference on Robotics and Automation*, pages 1967–1972, Wangshington, DC, USA, May 2002. IEEE.

[6] J. Lee, J. Park, and B. Lee. Turnover prevention of a mobile robot on uneven terrain using the concept of stability space. *Robotica*, 27(5):641–652, 2009.

[7] Y. Liu and G. Liu. Interaction analysis and online tip-over avoidance for a reconfigurable tracked mobile modular manipulator negotiating slopes. *IEEE/ASME Transactions on Mechatronics*, 15(4):623–635, 2010.

[8] D. Choi and J. Oh. Motion planning for a rapid mobile manipulator using model-based zmp stabilization. *Robotica*, 32(6), 2014.

[9] S. Lee, M. Leibold, M. Buss, and F. C. Park. Rollover prevention of mobile manipulators using invariance control and recursive analytic zmp gradients. *Advanced Robotics*, 26(11):1317–1341, 2012.

[10] R. Beranek, M. Karimi, and M. Ahmadi. A behavior-based reinforcement learning approach to control walking bipedal robots under unknown disturbances. *IEEE/ASME Transactions on Mechatronics*, 2021.

[11] T. G. Molnar, R. K. Cosner, A. W. Singletary, W. Ubellacker, and A. D. Ames. Model-free safety-critical control for robotic systems. *IEEE Robotics and Automation Letters*, 7(2):944–951, 2021.

[12] L. Cui, S. Wang, J. Zhang, D. Zhang, J. Lai, Y. Zheng, Z. Zhang, and Z. Jiang. Learning-based balance control of wheel-legged robots. *IEEE Robotics and Automation Letters*, 6(4):7667–7674, 2021.

[13] Y. de Viragh, M. Bjelonic, C. D. Bellicoso, F. Jenelten, and M. Hutter. Trajectory optimization for wheeled-legged quadrupedal robots using linearized zmp constraints. *IEEE Robotics and Automation Letters*, 4(2):1633–1640, 2019.

[14] J. Morales, J. L. Martinez, A. Mandow, J. Seron, and A. J. Garcia-Cerezo. Static tip-over stability analysis for a robotic vehicle with a single-axle trailer on slopes based on altered supporting polygons. *IEEE/ASME Transactions on Mechatronics*, 18(2):697–705, 2013.

[15] A. Argiolas, S. Casini, K. Fujio, T. Hiramatsu, S. Morita, M. Ragaglia, H. Sugiura, and M. Niccolini. Design, development and validation of a dynamic fall prediction system for excavators. In *2021 IEEE International Conference on Robotics and Automation (ICRA)*, pages 8523–8529. IEEE, 2021.

[16] K. Shigematsu, T. Tsubouchi, and Shigeru S. Tip-over prevention system based on motion prediction for teleoperated excavator. *Advanced Robotics*, 35(23):1438–1449, 2021.

[17] J. Song and I. Sharf. Time optimal motion planning with zmp stability constraint for timber manipulation. In *2020 IEEE International Conference on Robotics and Automation (ICRA)*, pages 4934–4940, Paris, France, May 2020. IEEE.

[18] L. Blackmore, M. Ono, and B. C. Williams. Chance-constrained optimal path planning with obstacles. *IEEE Transactions on Robotics*, 27(6):1080–1094, 2011.

[19] M. da Silva Arantes, C. F. M. Toledo, B. C. Williams, and M. Ono. Collision-free encoding for chance-constrained nonconvex path planning. *IEEE Transactions on Robotics*, 35(2):433–448, 2019.

[20] B. Du, J. Chen, D. Sun, S. G. Manyam, and D. W. Casbeer. Uav trajectory planning with probabilistic geo-fence via iterative chance-constrained optimization. *IEEE Transactions on Intelligent Transportation Systems*, 2021.

[21] J. Song and I. Sharf. Stability-constrained mobile manipulation planning on rough terrain. *Robotica*, 40(11):4090–4119, 2022.

[22] A. Geletu, M. Klöppel, H. Zhang, and P. Li. Advances and applications of chance-constrained approaches to systems optimisation under uncertainty. *International Journal of Systems Science*, 44(7):1209–1232, 2013.

[23] M. A. Patterson and A. V. Rao. Gpops-ii: A matlab software for solving multiple-phase optimal control problems using hp-adaptive gaussian quadrature collocation methods and sparse nonlinear programming. *ACM Transactions on Mathematical Software*, 41(1):1–37, 2014.

[24] A. Wächter and L. T. Biegler. On the implementation of an interior-point filter line-search algorithm for large-scale nonlinear programming. *Mathematical Programming*, 106(1):25–57, 2006.

[25] Miomir Vukobratović, Branislav Borovac, and Dragoljub Šurdilović. Zero moment point-proper interpretation and new applications. In *International Conference on Humanoid Robots*, pages 237–244, 2001.

Dr. Jiazhi Song received the B.S. and M.S. degree in Aeronautical and Astronautical Engineering from Purdue University, West Lafayette, IN, in 2016 and 2018, respectively. He received the Ph.D. degree in Mechanical Engineering at McGill University, Montreal, Quebec in 2023. His research interest include the optimal motion planning and control of intelligent vehicles and robots.

Antoine Petraki is currently in his fourth year pursuing a degree in Mechanical Engineering at McGill University in Montreal, Quebec, Canada. As a participant in the Summer Undergraduate Research in Engineering (SURE) program, he was given the opportunity to contribute to this research. He holds a particular interest in the fields of robotics and automation.

Dr. Brandon J. DeHart In general, Brandon's research interests span a wide range of topics connected to robotics, from tensegrity structures and bioinspired robot design to interactive architecture and morphological computation. Starting early in his academic career, Brandon has always strived to work on solving problems that will enable the widespread use of robots in entertainment, education, and exploration. At the University of Waterloo, he is currently a Sessional Instructor for Systems Design Engineering and Mechanical and Mechatronics Engineering, an Adjunct Assistant Professor in Electrical and Computer Engineering, and the Manager of the Waterloo RoboHub.

Dr. Inna Sharf is a professor in the Department of Mechanical Engineering at McGill University, Montreal, Canada. Sharf's research activities are in the areas of dynamics, control, motion planning and state estimation with applications to articulated machines, unmanned aerial vehicles and space systems. Sharf has published nearly 200 conference and journal papers on her academic research. She is an associate fellow of AIAA and a member of IEEE. She is currently on a reduced-load appointment at McGill (40%) and employed by FPInnovations at 60% FTE.